Development of Choked Flow in Variable Nozzle Radial Turbines

Andrés Tiseira[1], Luis Miguel García-Cuevas[1], Lukas Benjamin Inhestern[2] and Juan David Echavarría[1]

Abstract

In commonly applied one-dimensional choking models for radial turbines, choked flow is assumed to appear in the geometrical throat of each stator and rotor. Coupled and complex three-dimensional effects are not considered. In order to analyze the internal aerodynamic in a radial turbine at off design conditions and before carrying out experimental tests, which in the case of automotive turbocharger are limited by their compact size, computational fluid dynamics (CFD) simulations stand out as a useful tool. This paper presents the study of a variable geometry turbine (VGT) of a commercial turbocharger at off design conditions reaching choked flow, analyzing the presence of this limiting conditions in the stator and rotor under different operation points and VGT positions. Reynolds-averaged Navier-Stokes (RANS) and unsteady RANS simulation have been performed to obtain the flow structures in stator and rotor. The results reveal that the choked effective area mostly depends on the stator vane position and pressure ratio. For the closed VGT position a standing shock wave appears on the stator suction side and expands through the vaneless space. For the opened VGT position the flow is choked at the rotor outlet. However, the evolution of the choked area highly depends on the rotational speed and the secondary flow. A strong interaction with the tip leakage vortex has been identified.

Keywords

Turbocharging, Off-design, CFD, Internal Aerodynamics

1 Introduction

In order to improve the air quality and protect it in a sustainable manner between 2020 and beyond, the countries members of the European Union have set down regulations regarding to the emissions from various types of engines [1, 2]. For that reason, manufacturers are working on different systems as downsized engines with turbochargers to reduce the emissions of gaseous and particulate pollutants [3, 4]. To meet the engine power and torque targets, the downsized engine with the selected turbocharger represents an innovative concept capable of reducing a considerable percentage of the CO_2 emissions and improve the fuel economy [5, 6]. The turbocharger is key component to improve the engine performance, and different technology's exist to boost the engine [7]. One of them is the variable geometry turbine (VGT), which allows to improve the transient response as well as the torque deficiency at low speed conditions [8–10]. When the engine operates at low speed, the moving stator vanes, reduce the area of the nozzle, increasing the velocity of the exhaust gas and the energy consumed by the turbine [11]. However, this action results in a low volumetric efficiency [12] and high exhaust back pressure and can even lead to the development of shock waves in the stator.

Depending on the turbine geometry at closed vane position, the nozzle shock wave and nozzle clearance flow cause a high unsteady blade loading, according to Kawakubo et al.[13] the shock wave can penetrate deeply into the impeller LE and a strong positive pressure is exerted on the SS, then it diffracts on the PS. At open conditions, there is no presence of shock waves but the blade loading is less, however the nozzle clearance contributes to the formation of a strong shock wave on the mid-chord of the impeller SS producing a highly disturbed flow field. Furthermore, as stated by to Sato et al. [14] at closed vane position, the effects of shock waves and nozzle clearance flows on excitation force are intensified with increasing pressure ratio and the Mach number, while at opened vane position the excitation force is independent of the pressure ratio but depends on the density at the rotor inlet and the choked flows occurred near the rotor TE. In a turbine with the stator vanes closed and high inlet pressure, Zhao et al. [15] found that two shock waves appears, the first shock wave is generated near the throat of nozzle and it is followed by the second shock wave on the SS of the vane near the TE, existing a transonic region between them. Unsteadiness of the flow through the rotor is generated by the interaction between the blades and the second shock wave, which can be mitigated with the use of grooves on the SS of the vanes that generates an oblique shock and a reducing the pressure fluctuations [16]. A similar phenomenon appears in the air ramp intake of military aircrafts. Beside of reducing the efficiency [17, 18], the pressure fluctuation in the rotor blade can cause resonance and increase the possibility of high cycle fatigue fracture [19–22]. Such a risk can also be product of the propagation of secondary flow patterns as corner vortices and horseshoe vortices from the stator vane leading edge to the rotor [23, 24]. Rubechini et al. [25] highlighted that the strength of the unsteady interaction is related with the

[1]CMT - Motores Térmicos, Universitat Politècnica de València, Spain
[2] Institute of Aeronautics and Astronautics, TU Berlin, Germany

Corresponding author:
Juan David Echavarría, CMT - Motores Térmicos, Universitat Politècnica de València, Valencia 46022, Spain.
Email: juaecol@mot.upv.es

pattern of the shock wave at the region between the nozzle and the rotor, such pattern depend on the nozzle geometry. The shock impinging the rotor LE result in a strong pressure fluctuations and generating a high entropy rate within the rotor. The vibrations generated by the pressure fluctuations can be measured by the tip-timing method in which the deflection causes the blade to pass a series of laser probes earlier or later than a predicted time, hence the difference of this times can be used to calculate the deflection from the initial position for each individual blade [26, 27]. According to Sauret [28] even if the turbine was created for subsonic flow, when operates at high pressure ratios the choked flow can appear in the nozzle together with a small separation region near the rotor LE.

A lot of studies including the aforementioned have been carried out with computational fluid dynamic (CFD) tools, and validated with experimental test depending on the possibility of install the measuring instruments inside of the compact components of the turbocharger due to space limitations, being necessary in some cases scale the geometry [29, 30] to analyze the effects on the separation bubble and tip leakage flow, as well as the measurement of the pressure and velocity inside the stator using pitot tubes [31].

Thus, CFD is in many cases a useful and reliable tool to characterize the internal aerodynamic of the turbine, at off-design operational points, where the mass flow can be extremely low and the turbine can work with negative efficiency [32]. Other numerical studies with the intention to propose one-dimensional loss models and design procedures in radial turbine have focused on the losses generated by the rotor tip leakage, which can increase considerable with a small increase in the local blade loading, moreover the increase in the tip gab height affect more the turbine efficiency than the reduced mass flow [33, 34]. Regarding to the nozzle leakage flow, Zhao et al. [18] identified that the increase in the endwall clearance lead to a significant rise in Mach number throughout the chord, due to the reduction of the boundary layer effects in this region.

In order to have a deeper understanding of the flow behavior at off-design conditions with high pressure ratios (PRs) reaching the chocked flow, CFD simulations are conducted in this paper. The flow pattern in the stator and rotor passage of a variable geometry turbine operating at different speeds and pressure ratio is presented and gives first approximation of the internal phenomena before carrying out complex experimental tests in a turbocharger gas stand. Furthermore, the results of this paper can contribute to the future development of one-dimensional modeling to estimate excitation forces in a fast and precise way during the turbine design process [14] and also to elaborate extrapolation models of the turbine map at high expansion ratio as the models presented by Serrano et al. [35], Romagnoli et al. [36] or Meroni et al. [37], due to the difficulty to obtain measurements under these off-design conditions. These kind of models can be connected directly to the one-dimensional whole engine models to achieve an optimum engine-turbocharger matching and engine performance [38, 39].

In the first part of this paper, the setup used for obtaining steady and unsteady results with different pressure ratios, stator vane positions and rotational speeds is described. Second, the global performance parameters are presented after accomplishing a mesh analysis. The following sections present the flow analysis and characteristics for the stator and rotor at chocking conditions. Afterward, an exergy analysis for the entire turbine domain is explained. Finally, certain aspects are highlighted and concluded.

2 Geometry Description

Table 1. Turbine geometry parameters.

	Stator	Rotor
Blade number	11	9
Inlet diameter	-	41 mm
Outlet diameter	-	38 mm
Tip clearance	0.2 mm	0.36 mm to 0.4 mm
Nozzle vane height	7.7 mm	-
Chord length	18.95 mm	-
Blade angle α (VGT opening)	78.34° (10%), 53.45° (80%)	-
Outlet blade angle	-	59°

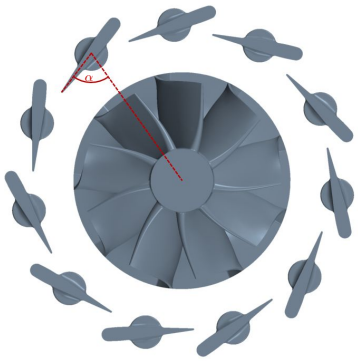

Figure 1. Stator and rotor geometry [32].

A commercial variable geometry turbocharger turbine, designed for 2L diesel engines, has been used for this study. The turbine was previously studied at different conditions up to low mass flows and even negative turbine power output by Serrano et al. [32, 34, 40]. The stator passage owns eleven stator vanes while the rotor has 9 blades, which are depicted in Figure 1. Table 1 present the dimensions and features of the stator and rotor passage. In the simulated fluid domain the inlet and outlet ducts, the volute, stator and rotor are included as illustrated in Figure 2. The inlet duct has a length of six diameters, which results in a length equal to 200 mm, while the length of the outlet duct is around nine diameters resulting in a length of 400 mm being long enough to include the experimental measurement section in the domain. The probe section are placed at the same location of experimental measurement probes, which are located according to turbocharger gas stand test code

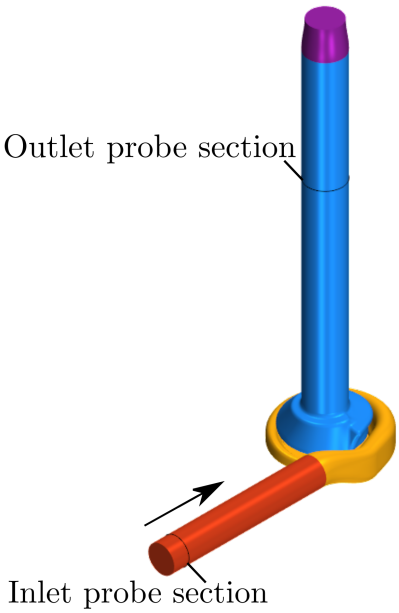

Figure 2. Computational domain [32].

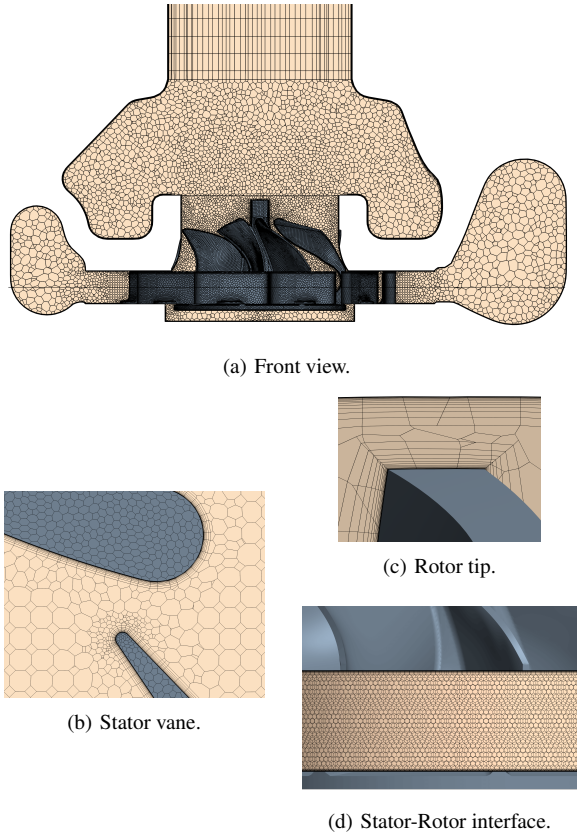

(a) Front view.

(b) Stator vane.

(c) Rotor tip.

(d) Stator-Rotor interface.

Figure 3. Section view of the mesh.

[41]. Furthermore, downstream of the outlet probe section a convergent duct with an exit diameter equal to the wheel outlet diameter is part of the computational domain. This allows to set a similar static pressure in the outlet of the domain as it would expect in the outlet of the rotor. This is more suitable for the study of the chocked flow in the rotor outlet as similar downstream pressures can be obtained. With the aim of analyzing the choking phenomena in the stator and rotor, two VGT positions are considered in this paper. The first one is a VGT opening of 10% representing a closed position and the second one is 80% representing a widely opened position. In the simulations conducted by Serrano et al. [32] the VGT positions were stepwise varied with the highest pressure ratio until the reduced mass flow was matched with the selected points of the experimental test [42]. Those particular VGT positions were experimentally assessed in previous work up to low flow conditions and will be maintained in this investigation to allow consistent map information. From this point forward, 10% and 80% VGT opening will be referred as closed and open position respectively.

3 Numerical Setup

In this research, to examine the internal flow field of the turbine under varying conditions the CFD software Star-CCM+ 2019.1 (Build 14.02.010-R8) was employed. The fluid was considered as an ideal and compressible gas. Since chocked flow with occurring shock waves is in the focus of this research, the density based coupled solver has been chosen [43]. Two types of solutions of the time domain are shown in this paper. First, steady Reynolds averaged Navier Stokes (RANS) simulations with a frozen rotor and second, unsteady RANS simulations for selected operating conditions were run. A frozen rotor without mixing plane was chosen in the steady simulations to avoid vanishing of rotor-stator interactions. To obtain turbulence closure the k-ω SST model [44] has been selected, as it is widely recommended and well validated for radial turbomachinery in the literature [45–48] even under transonic and supersonic conditions [21, 49, 50]. Furthermore, with a finer grid and improved resolution in the near wall region the model generates results that agree well with the experimental data [51, 52]. Compering with different turbulent models the k-ω SST model predictions are closer to the experimental value in terms of wall pressure distribution [53]. Under supersonic conditions the flow field structure, surface pressure, velocity profiles and the overall features of these complex flow fields can be predicted [53, 54]. However, the SST model needs improvement on the wake flow [55]. The entire fluid domain, which consists of the inner volume of the volute, stator and rotor, has been discretized by means of an unstructured polyhedral mesh, whereas for the inlet and outlet duct a generalized cylinder mesher has been used to generate an extruded mesh along the duct's length as can be seen in the Figure 3 (a). Prism layers have been generated in the boundary layer region allowing to capture viscous gradients close to the wall, a mesh with similar characteristics was used by Serrano et. al [32] aiming a low Reynolds criteria, nevertheless higher mass flow with elevated Reynolds number are analyzed in the presented work.

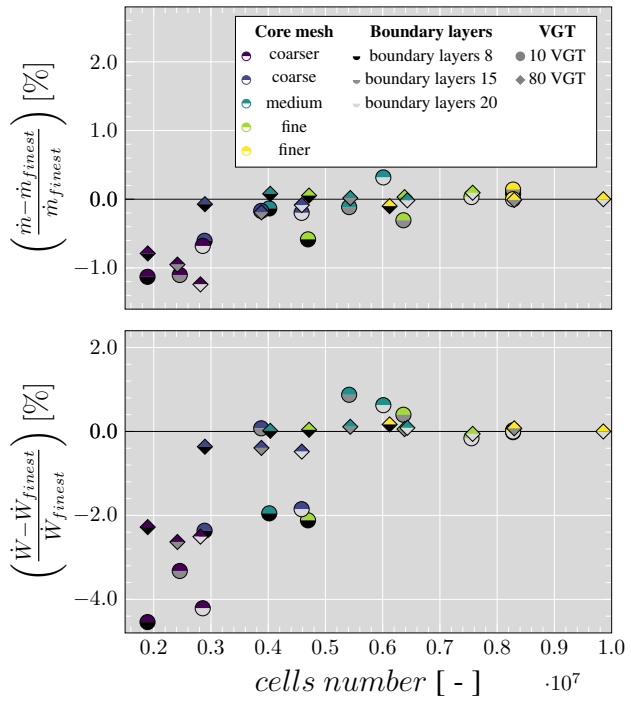

Figure 4. Variation of mass flow and turbine power with different mesh configurations relative to the finest simulated mesh for opened and closed position.

To obtain a suitable number of cells an extensive mesh sensitivity analysis study has been carried out to achieve a grid independent numerical solution. In this manner, the operation point at 3882 $rpm/\sqrt{K}$, which will be considered as the lower speed, and a high pressure ratio for both, closed and opened VGT positions has been selected to find a grid size that has a good enough resolution to cover all simulated operating conditions and gives reliable results [56, 57]. The core and boundary layers of the volute, stator and rotor have been changed independently using five different core mesh densities from coarser to finer and three boundary layer meshes. The inlet and outlet duct has been meshed with a core of medium density and fifteen prism layers in the boundary layer having a y^+ of 0.46 and 0.34 respectively for the closed position, while for the opened position the y^+ is 1.12 and 0.84 respectively. Thus, overall 15 types of meshes for closed VGT position and other 15 meshes for the opened position have been generated. Figure 4 depicts the mesh analysis carried out evaluating the relative variation of the mass flow and power with respect to the finest mesh, which has the highest core mesh density and 20 prism layers in the boundary layer. All generated meshes have a medium y^+-value close to one to fulfill the low Reynolds criteria. The change in number of prism layers in the boundary layers does not affect significantly the mass flow in both VGT positions as it does with the power for the closed position. At opened VGT position the mass flow and power do not experience changes of high order using the three different boundary meshes. Furthermore, the power at the closed position fluctuates more than at the opened position when the number of prism in the boundary layer varies. The biggest difference take place with the coarser and the coarse cores, while the variations with the medium and fine core are quite similar. However, the computational time of the fine core can be considered as high. Consequently, the mesh with a medium core and 15 cells to resolve the boundary layer has been chosen for the calculation of the different operation points that will be presented in the following sections. This mesh owning 5.4 million cells and the expansion ratio in the prism layer mesh has been chosen to be 1.3. For the closed VGT position a mean y^+ of 0.7 has been achieved for the turbocharger geometry (volute, rotor, stator & outlet volume), while the opened VGT position presents a mean y^+ of 1.3.

3.1 Boundary Conditions

Simulations were conducted with the two aforementioned stator vane positions with two different reduced turbine speeds of 3882 $rpm/\sqrt{K}$ and 8421 $rpm/\sqrt{K}$, which can be referred as lower and higher speed respectively. Nevertheless, for the opened VGT position a rotational speed of 5830 $rpm/\sqrt{K}$ called middle speed was additionally simulated. For the steady and unsteady cases, the turbine total inlet temperature is set as a boundary condition with a value of 340.55 K. Such a low temperature has been chosen, because previous experimental measurements were executed in quasi-adiabatic conditions and thus it is possible to maintain similar conditions of the Mach number. Future measurements will be done in choked condition as an extension of the same map under the same measurement principle. For the same reason adiabatic walls can be applied in these simulations [32]. Furthermore, turbines operating with low inlet temperature can be found in Organic Rankine cycle [58, 59], air cycle heat pump [60, 61] and in the environmental control system (ECS) of commercial aircraft [62, 63]. The outlet static pressure was kept constant at 1 bar. The inlet total pressure was varied from moderate up to high total pressures in order to achieve iso-speed lines with developing choke conditions. For unsteady flow results, the time step size has been selected as the time that takes the turbine wheel to rotate two degrees depending on the rotational speed [32, 56]. This size corresponds to 180 time steps per rotor revolution. Furthermore, 20 inner iterations steps were necessary to bring each time step to convergence looking at the residuals of inner iterations and applying a low CFL number of 2. The convergence has been reached after around 3 rotor rotations for the cases of low speed and after around 8 revolutions at high speed independent of the VGT position.

4 Results and Analysis

To deepen the understanding of the choked flow this study is divided as follows. First the trend and characteristics of the turbine map are analyzed. The turbine map was obtained from the steady flow results, moreover, based on these results two operating points of each speed line were chosen to demonstrate the flow pattern just during the development of passage choking and with fully choked characteristics. These points were simulated in URANS simulations. Thus, global performance parameter were evaluated with both steady and unsteady state simulations to assess the importance of unsteady effects caused by blade row interaction on the performance characteristics. Here, the transient simulation

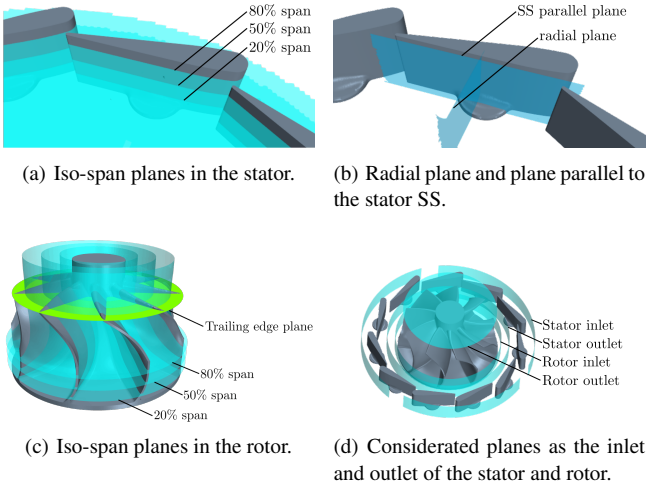

(a) Iso-span planes in the stator.

(b) Radial plane and plane parallel to the stator SS.

(c) Iso-span planes in the rotor.

(d) Considerated planes as the inlet and outlet of the stator and rotor.

Figure 5. Considered planes in the stator and rotor for following data analysis.

Table 2. Evaluated pressure ratio URANS simulations.

VGT [%]	$N_{red.}$ $[\frac{rpm}{\sqrt{K}}]$	$\pi_{turb.}$ [-]		$\pi_{stat\,t,t}$ [-]	η_{stat} [-]
10	3882	lower	2.95	1.21	0.69
10	3882	higher	5.16	1.34	0.83
10	8421	lower	2.64	1.12	0.73
10	8421	higher	4.48	1.22	0.71
80	3882	lower	2.55	1.06	0.87
80	3882	higher	3.53	1.05	0.88
80	5830	lower	2.69	1.05	0.87
80	5830	higher	3.82	1.05	0.89
80	8421	lower	2.75	1.05	0.86
80	8421	higher	4.17	1.05	0.86

results have been time-averaged over one rotor rotation. The plane in the rotor TE depicted in Figure 5-(c) has been used to process particular fluid numbers for this analysis. Second, the flow behavior through the stator is presented and finally the study focuses on the flow conditions in the rotor. The three-dimensional flow pattern in the stator and rotor is analyzed by means of the planes shown in Figure 5, according to Drela and Youngren [64].

4.1 Performance Characteristics

The reduced mass flow and the isentropic efficiency total to static considered for this study are defined in Equation 1 and Equation 2 respectively, where the term $\pi_{turb.}$ is the total to static pressure ratio between the inlet probe section and the outlet probe section depicted in Figure 2. In these sections, the pressure was evaluated by using mass flow averaging.

$$\dot{m}_{red.,in} = \frac{\dot{m} \cdot \sqrt{T_{t,in}}}{p_{t,in}} \tag{1}$$

$$\eta_{t,s} = \frac{T_{t,in} - T_{t,out}}{T_{t,in} \cdot \left[1 - \left(\frac{1}{\pi_{turb.}}\right)^{\frac{\gamma-1}{\gamma}}\right]} \tag{2}$$

$$\eta_{stat} = \left(\frac{u_{stat\,out}}{u_{stat\,isen,out}}\right)^2 \tag{3}$$

$$u_{stat\,isen,out} = \begin{cases} \text{If } \frac{1}{\pi_{stat\,t,s}} > \left(\frac{2}{\gamma+1}\right)^{\frac{\gamma}{\gamma-1}} \\ \sqrt{2 \cdot c_p \cdot T_{stat\,t,in} \cdot \left[1 - \left(\frac{1}{\pi_{stat\,t,s}}\right)^{\frac{\gamma-1}{\gamma}}\right]} \\ \text{If } \frac{1}{\pi_{stat\,t,s}} \leq \left(\frac{2}{\gamma+1}\right)^{\frac{\gamma}{\gamma-1}} \\ \sqrt{2 \cdot c_p \cdot T_{stat\,t,in} \cdot \left(\frac{\gamma-1}{\gamma+1}\right)} \end{cases} \tag{4}$$

The results of the total to static pressure ratio $\pi_{turb.}$ for the unsteady simulations are listed in the Table 2 together with the designation as lower or higher, that from here will be considered. Furthermore, in the same table, the total to total pressure ratio in the stator ($\pi_{stat\,t,t}$) calculated between the inlet probe section and the stator outlet plane (see Figure 5-(d)) is presented, as well as the stator efficiency defined according to the Equation 3 and Equation 4, where $\pi_{stat\,t,s}$ is the total to static pressure ratio in the stator. As can be seen, the pressure ratio in the stator does not change significantly when the pressure at the inlet of the turbine or the rotational speed increases, due to the fact that the function of the vanes is to direct the flow toward the rotor where the main expansion take place as well as increase the velocity of the flow when the vanes are closed. In Figure 6, the reduced mass flow and the total-to-static efficiency of all simulated operating points in steady and unsteady simulations are depicted. Here, also the experimental results of previously performed standardized experiments of the same turbocharger turbine at various rotor speeds are shown [42]. These data were obtained in the typical measurement range of automotive turbocharger turbines, which does not cover such high expansion ratios as they were observed in this study. However, the results can be used to obtain a qualitative validation of the simulation results. While the experimental results of 3882 $rpm/\sqrt{K}$ and 5830 $rpm/\sqrt{K}$ can directly be compared, the results of higher speeds up to 7456 $rpm/\sqrt{K}$ are shown to allow an estimation of trends towards higher speeds. The trends and magnitudes of simulated reduced mass flows and efficiencies at lower pressure ratio can be confirmed by those data for both VGT positions. Additionally, simulated and experimental efficiencies are comparable with the demonstration against the blade speed ratio (BSR). Here, it can be seen that the simulated efficiencies match well the experimental measurement trends. This way, e.g. the higher simulated speed at opened VGT position matches well the experimental data at higher BSRs. According to the observations made by Serrano et al. [65] an overlapping of speed lines in the BSR plots can be expected towards higher BSR when the stator vanes are opened, while at closed VGTs the speed lines of isentropic efficiency total to static are wider spread. Serrano et al. [35] noted this last trend in a previous study.

Table 3. Comparison of RANS and URANS results.

VGT [%]	$N_{red.}$ [$\frac{rpm}{\sqrt{K}}$]	$\pi_{turb.}$ [-]	Dev. $\dot{m}_{red.}$ [%]	$\Delta\eta_{t,s}$ [% points]
10	3882	low	-1.63	0.91
10	3882	high	-3.52	0.63
10	8421	low	-3.42	2.21
10	8421	high	-2.02	0.52
80	3882	low	0.06	-0.11
80	3882	high	0.24	-0.10
80	5830	low	0.85	-0.51
80	5830	high	0.47	-0.13
80	8421	low	-0.01	-2.00
80	8421	high	-0.71	-0.31

Future measurement results will extend the map to supply further experimental validation at high PR. In line with the common literature, the reduced mass flow starts to stagnate as soon as full choking is achieved in the turbine, as it can be found in different publications showing measurements at opened and closed VGT positions [38, 66, 67]. As it can be seen in Table 3, the differences in the reduced mass flow between the steady and unsteady conditions are small, being less than 1% for each reduced speed at opened vane position. Nevertheless, at closed vane position the differences are higher and the maximum difference is presented in the operating point at lower speed and higher pressure ratio with a value of -3.52%. With regards to the efficiency as shows Figure 6-(b), the maximum change take place at higher speed and lower pressure ratio, with -2.00% points at opened vane position and 2.21% points at closed position. For the rest of the unsteady points the deviations from the steady cases are less than 1% points. Thus, the reproduced trends and overall rather low deviations, allow to evaluate the trends of the turbine map by mean of the frozen rotor steady simulations. For a further evaluation, the rotor has been rotated by 20 deg, which corresponds to the highest possible deviation of the rotor geometry with 9 blades. Results show less than 0.01% points of deviation in the efficiency and around 0.1% deviation in the simulated mass flow. Both values can be considered as negligible variations, which demonstrate low impact of the simulated rotor position in RANS simulations.

The mass flow map with closed vane position shown in Figure 6-(a) indicates that the flow under the conditions of the higher iso-speed reaches the choking condition at higher pressure ratios than the lower speed. At a pressure ratio of 5.6 the operating point joins the speed line of the lower speed, which shows stagnated reduced mass flow after reaching an expansion ratio of around 5. On the other hand, the speed line of the opened VGT presents separately choked lines, as it typically can be found for opened VGT positions. However, the middle speed is located very close to the lower simulated speed when the flow is choked.

Regarding to the effects on the efficiency, the development of the choked flow is mainly related with the pressure ratio. Thus, when the pressure ratio is increased at closed VGT and lower rotational speed the efficiency starts to decrease until certain point after which remains constant as is depicted in

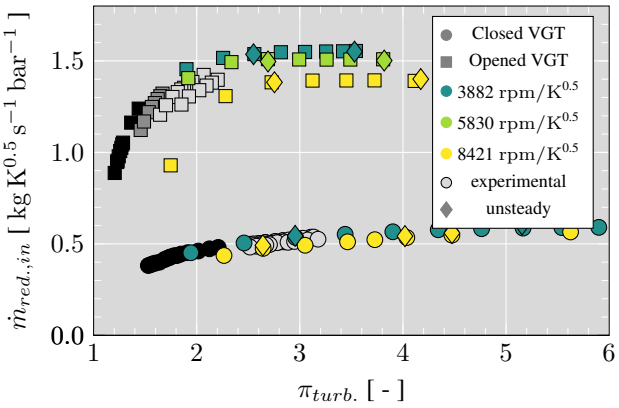

(a) Reduced mass flow map.

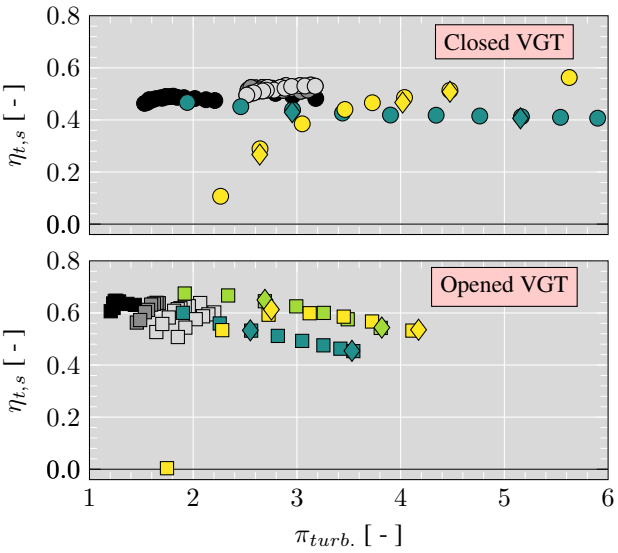

(b) Efficiency vs. expansion ratio map.

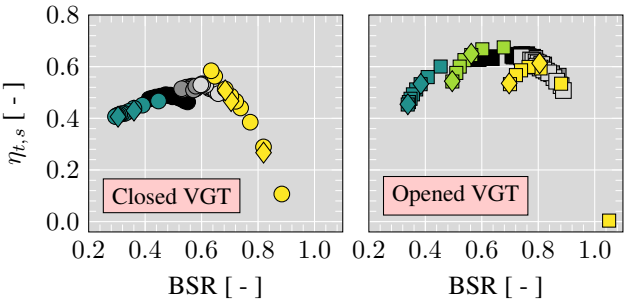

(c) Efficiency vs. blade-speed-ratio map.

Figure 6. Turbine map based on steady and unsteady results; experimental 3882 $rpm/\sqrt{K}$: black; experimental 5830 $rpm/\sqrt{K}$: dark gray; experimental up to 7456 $rpm/\sqrt{K}$: light gray; simulated: colored.

Figure 6-(b). On the contrary at higher speed the efficiency increases as the pressure ratio increases. Nevertheless, in both cases the reduced mass flow stagnates at a pressure ratio less than the pressure ratio at which the efficiency starts to keep constant. At opened VGT the efficiency reaches a maximum peak for each rotational speed, then as the pressure ratio continues increasing, the efficiency drops.

In one-dimensional modeling the rotor is typically modeled as a nozzle, where the throat is located directly

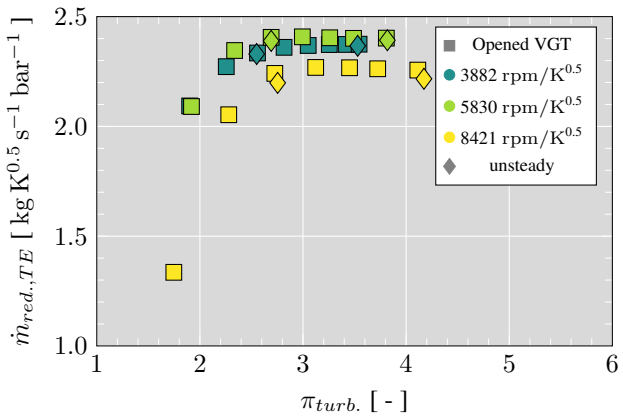

Figure 7. Reduced mass flow based on the mean total temperature and total pressure in the rotor outlet.

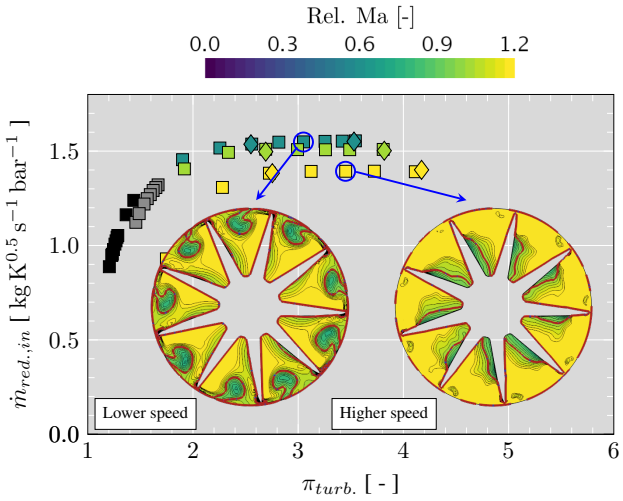

Figure 8. Relative Mach number with opened VGT position and operating point of choked passage flow at the rotor TE plane; red line: $Ma_{rel.} = 1$.

in the rotor outlet. In this case, choking is reached when a relative Mach number of one is obtained in the rotor outlet. Consequently, the reduced mass flow, based on the numbers obtained in the corresponding rotor TE plane, is maintained at the same value for all reduced speeds. Taking advantage of following presented results, it can be said that for the opened VGT position only the rotor passage becomes choked. To analyze the phenomenon in more detail, the reduced mass flow in Equation 5 based on total numbers extracted close to the rotor TE is depicted in Figure 7. Here, the flow did not experience high shock losses in the main passage yet.

$$\dot{m}_{red.,TE} = \frac{\dot{m} \cdot \sqrt{T_{t,TE}}}{p_{t,TE}} \tag{5}$$

Here, $\dot{m}_{red.,TE}$ appears not to stagnate in the same order as in the previously analyzed map of the overall reduced mass flow. The middle speed converges to a higher value than the others, although it is close to the value of the lower speed. According to traditional one-dimensional modeling, a choking at the same reduced mass flow in the relative frame would be expected close to the rotor outlet. However, the radial turbine owns a highly three dimensional "non-ideal" geometry with tip leakage flow, as it can be seen in Figure 8 for the TE plane, which has been introduced in Figure 5-(c). The shown operating points are the first points after stagnation in the $\dot{m}_{red.,TE}$ map. It is visible that the majority of the passage is choked. However, the tip leakage vortex causes locally subsonic flow, which avoids complete rotor choking close to the rotor TE. Over the choked area a relative Mach number above 1 can be identified, since the flow becomes further accelerated after the non-idealized turbine rotor throat. At higher speed, the sub-sonic regions at the hub close to the PS result from the location of the TE plane. At these low spans the rotor trailing edge is further downstream of the demonstrated plane. However, the flow further accelerates along the PS and becomes fully choked although it is not visible in this representation. This will be further illustrated in following analysis of the three-dimensional flow. The average relative Mach number in the TE plane achieves with 1.13 a 7% lower value for the lower speed than the one at higher speed with a relative Mach number of 1.22.

According to Equation 6 the reduced mass flow decreases for increasing Mach numbers above 1.

$$\dot{m}_{red.} = A \cdot \sqrt{\frac{\gamma}{R}} \cdot Ma \cdot \left(1 + \frac{\gamma - 1}{2} \cdot Ma^2\right)^{-\frac{\gamma+1}{2(\gamma-1)}} \tag{6}$$

Hence, the reduced mass flow extracted close to the TE is higher when the passage flow is choked but the tip leakage flow generates zones of lower Mach numbers, reducing the mass flow averaged Mach number in this section. To estimate the impact on the overall reduced mass flow, as defined in Equation 1, some simplifications can be made. Assuming that the main part of the work is extracted until the TE plane, the turbine inlet total temperature can be reformulated in dependence of the total temperature in the plane at the TE, the efficiency and the turbine expansion ratio:

$$T_{t,in} = \frac{T_{t,TE}}{1 - \eta_{t,s} \cdot \left[1 - \left(\frac{1}{\pi_{turb.}}\right)^{\frac{\gamma-1}{\gamma}}\right]}. \tag{7}$$

To achieve a dependency of the total temperature in the relative reference frame, the Equation 7 can be reformulated to:

$$T_{t,in} = \frac{T_{t,rel.,TE} \cdot \frac{1+\frac{\gamma-1}{2} \cdot Ma^2_{TE}}{1+\frac{\gamma-1}{2} \cdot Ma^2_{rel.,TE}}}{1 - \eta_{t,s} \cdot \left[1 - \left(\frac{1}{\pi_{turb.}}\right)^{\frac{\gamma-1}{\gamma}}\right]}. \tag{8}$$

The relation between total pressure just before the development of shocks and total inlet pressure can be drawn:

$$p_{t,in} = p_{t,rel.,TE} \cdot \pi_{t,rel.,TE}. \tag{9}$$

Indeed, when the pressure is measured further downstream this pressure ratio will additionally depend on the area ratio and swirl, related to the rotational speed of the turbine and shock losses. Substituting Equation 8 and Equation 9 in the turbine map value of the reduced mass flow according to

Equation 1, the following relation is derived:

$$\dot{m}_{red.,in} = \frac{\frac{\dot{m}\cdot\sqrt{T_{t,rel,TE}}}{p_{t,rel.,TE}} \cdot \sqrt{\frac{1+\frac{\gamma-1}{2}\cdot Ma^2_{TE}}{1+\frac{\gamma-1}{2}\cdot Ma^2_{rel.,TE}}}}{\pi_{t,rel.,TE}\cdot\sqrt{1-\eta_{t,s}\cdot\left[1-\left(\frac{1}{\pi_{turb.}}\right)^{\frac{\gamma-1}{\gamma}}\right]}}. \quad (10)$$

The first factor in the numerator can be recognized as the reduced mass flow calculated based on the conditions at the rotor TE. This highlights, the direct impact on the distribution of speed lines in the global reduced mass flow map. The second factor in the numerator takes the relative Mach number into account. This way the effect of the tip leakage flow strengthens the relative distance between the speed lines, when they are translated to the traditional map value. In the denominator $\pi_{t,rel.,TE}$ can be found.

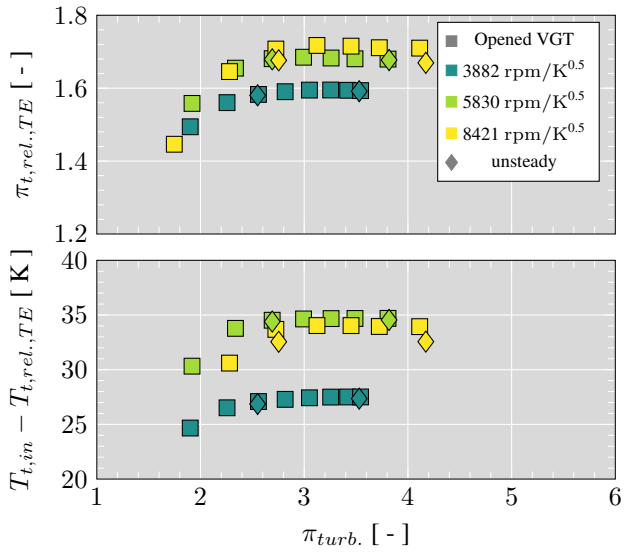

Figure 9. Total pressure ratio and total temperature difference of the inlet properties and relative numbers at rotor TE plane.

In Figure 9 it can be seen how the total pressure ratio $\pi_{t,rel.,TE}$ starts to stagnate and to maintain its value at a turbine pressure ratio $\pi_{turb.}$ around 3. Here, the pressure ratio of the higher speed archives bigger values. This might cause a natural spreading of the speed lines even when no significant change of the tip leakage flow pattern can be identified. The final map value then further depends on the turbine pressure ratio and the turbine efficiency. At lower speed, the total temperature delta $T_{t,in} - T_{t,rel.,TE}$ stagnates at a slightly lower turbine pressure ratio, than the reduced mass flow at the rotor TE in the rotational frame. This could confirm the observation of a mostly choked passage flow. The possible variation of tip leakage flow towards higher pressure ratios has rather small impact on the extraction of specific enthalpy in the rotor passage [34, 40, 68], although it significantly contributes to pressure losses and thus, efficiency penalties. Further, it is worth highlighting that the total temperature difference $T_{t,in} - T_{t,rel.,TE}$ is the highest when the reduced speed is intermediate. It can be concluded that the tip leakage vortex omits the complete choking of the rotor passage outlet, which results in the increase of local and overall reduced mass flow at lower speeds, where a

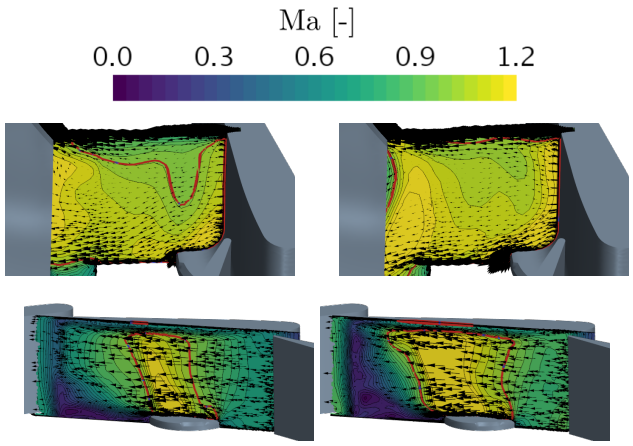

(a) Higher speed at higher PR. (b) Lower speed at higher PR.

Figure 10. Mach number of URANS simulations at a radial plane and at a plane parallel to the stator SS (see Figure 5-(b)) with closed VGT position; red line: $Ma = 1$.

stronger tip leakage vortex can be observed. Biggest parts of the passage are aerodynamically choked, so that the relative values of the pressure ratio and total temperature delta up to the rotor TE remain constant. Further, when heat transfer is considered, the adiabatic efficiency in Equation 10 can be substituted with the non-adiabatic efficiency, highlighting the impact of heat transfer on the choking limitation. This dependency may be further analyzed in the future experimental campaign with a comparison of quasi-adiabatic and hot measurements.

4.2 *Stator Flow Characteristics*

Depending on the stator vane position the choking occurs in the region of the stator or rotor. Thus, for the closed VGT position the shock only appears in the stator according to the results of each one of the evaluated planes at 20, 50 and 80% span. It was found that the area of the supersonic regions in these planes change slightly for each span despite of having a straight blade, the main reason for this result is the interaction of the primary flow with the stator blade tip leakages and the geometry of the stator's penny (also referred to as "button", it is the cylindrical platform feature of each variable stator vane) as can be seen in the Figure 10 with the velocity vectors in these regions. The presence of the penny generates vortexes, increasing the losses [69, 70]. However, it should be taking into account that the secondary losses appear to decrease with increasing Mach numbers [71]. Nevertheless, the more relevant changes that are aim of this study only occur when the pressure ratio or the rotational speed varies. Hence, snapshots of the unsteady results are shown only at 50% span. Figure 11 depicts how the flow in the vaneless space (the region between the stator SS and the rotor inlet) becomes choked with increasing pressure ratio for the two selected speed lines. At a higher reduced speed of $8421\,rpm/\sqrt{K}$ with higher PR, a supersonic pocket is developed at around 0.63 normalized chord length on the suction side of the stator blade. The supersonic pocket expands up to close to the rotor inlet. There, another supersonic acceleration takes place, which

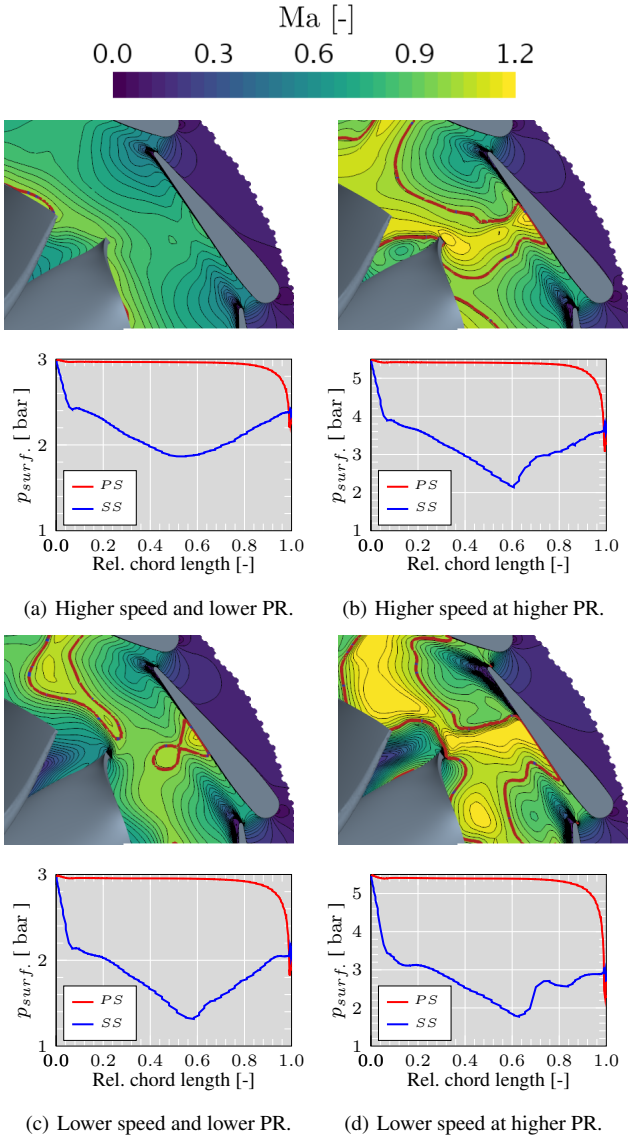

(a) Higher speed and lower PR. (b) Higher speed at higher PR.

(c) Lower speed and lower PR. (d) Lower speed at higher PR.

Figure 11. Mach number and stator vane pressure profile snapshots of URANS simulations at 50% span of the stator passage with closed VGT position; red line: $Ma = 1$.

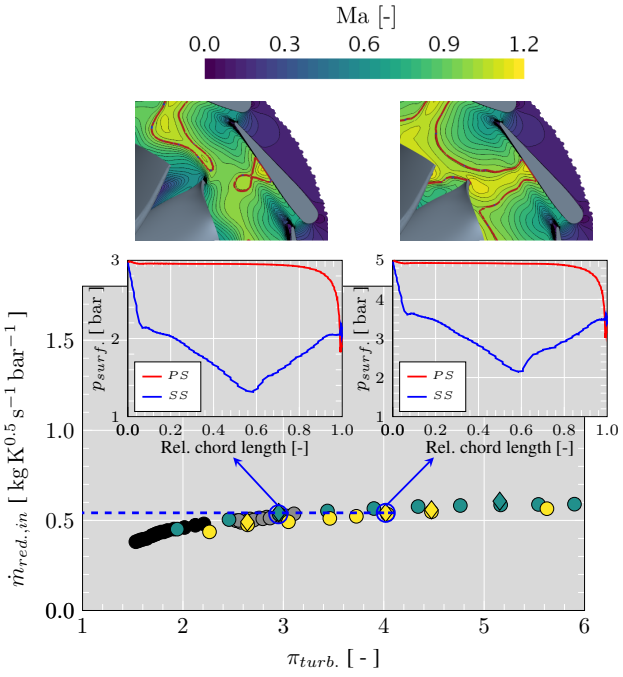

Figure 12. Mach number and stator vane pressure profile snapshots for two operating points of URANS simulations with the same reduced mass flow, closed VGT position and at 50% span of the stator passage; left: lower speed; right: higher speed; red line: $Ma = 1$.

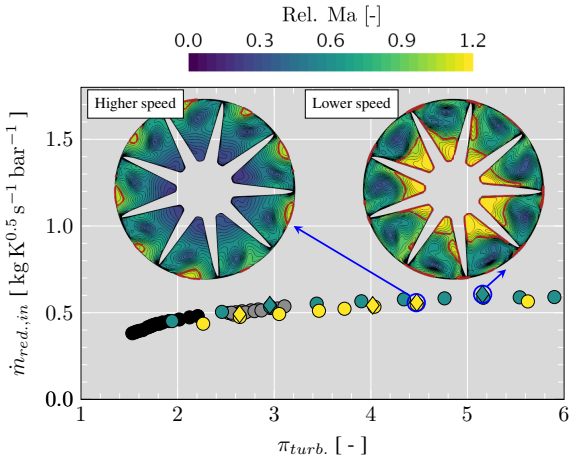

Figure 13. Relative Mach number snapshots of URANS simulations with closed VGT position higher expansion ratio close to the TE of the rotor; red line: $Ma_{rel.} = 1$.

connects the pockets of two neighboring stator blades. At this closed VGT position, the distance from blade curvature on the SS to the rotor inlet first shrinks and then augments again. This generates a throat were supersonic flow develops. From this throat the flow decelerates more due to the increase of positive radial velocity. In the pressure profiles, a sudden rise identifies a shock generating a sudden flow deceleration, as well as entropy and loss generation [72]. In comparison, the completely unchoked solution at low pressure ratio owns a rather smooth pressure profile. The simulated operating points at lower reduced speed of $3882\,rpm/\sqrt{K}$ represent points which are closer to choke and fully choked. Here, the appearance of the supersonic pocket can be observed at the results of lower pressure ratio. The supersonic area flow does not expand up to the rotor inlet yet and seems to be discontinuous on one stator vane, while the neighboring pocket is already reaching the rotor inlet and seems to interact with the rotor blade.

To analyze the unbiased impact of the rotational speed, two simulations where the reduced mass flow has been maintained at low and at high speed, as Figure 12 depicts, were analyzed. The pressure profiles look very similar in their qualitative shape, which confirms the aerodynamic similarity of both operating points around the stator vane. In the Mach number distribution the supersonic pocked at the vane SS is located at the same position. However, the overall Mach number distribution has a significantly different pattern for both speeds. At higher speed, the supersonic region reaches the rotor inlet on the SS and hits the LE joining with the contiguous supersonic region. At lower

speed, the flow has much less flow with velocities above the sonic limit close to the rotor and the shock wave on the vane SS propagates less towards the rotor inlet.

In order to consider the effects of the rotor rotation, one blade passing at closed VGT position and higher pressure ratio was analyzed. The intensity of the supersonic pocket close to the vane SS does not present any variation at higher speed, whereas at lower speed the extension of the choked region varies. For both speeds the connection between the two neighboring pockets disappear after the blade passes the entire vane. It is worth highlighting that at no operating point shock waves appear in the perpendicular cross section between the stator TE and the neighboring vane. To reach choking conditions in the stator passage, the vanes neede to be closed much further up to 0% VGT opening, which does not occur in real operational conditions.

4.3 Rotor Flow Characteristics

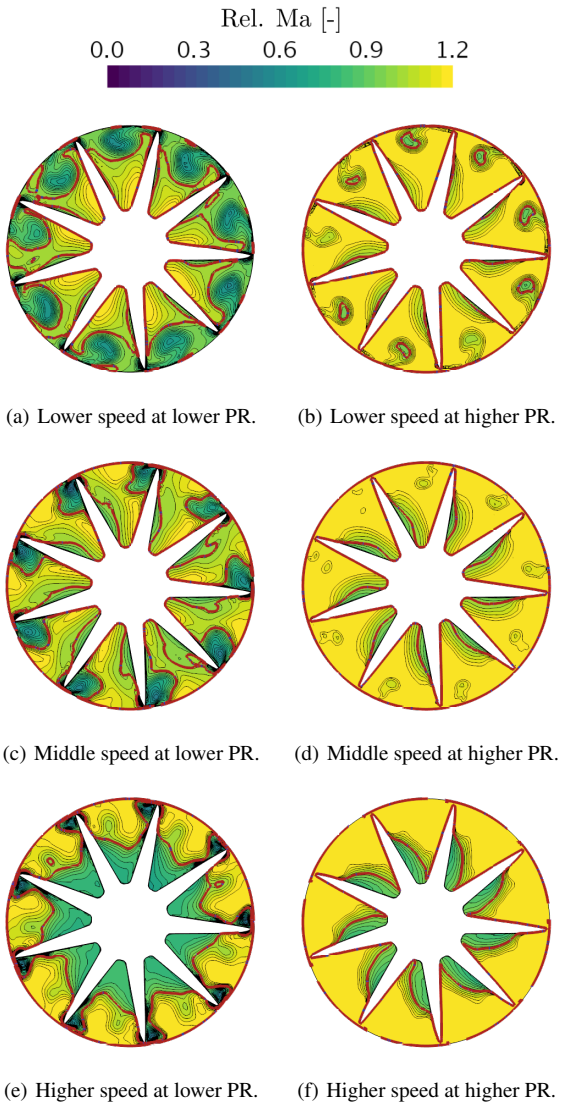

(a) Lower speed at lower PR. (b) Lower speed at higher PR.

(c) Middle speed at lower PR. (d) Middle speed at higher PR.

(e) Higher speed at lower PR. (f) Higher speed at higher PR.

Figure 14. Relative Mach number snapshots of URANS simulations with openes VGT position; red line: $Ma_{rel.} = 1$.

With closed VGT position, no supersonic flow is present close to the rotor TE plane under operation conditions of

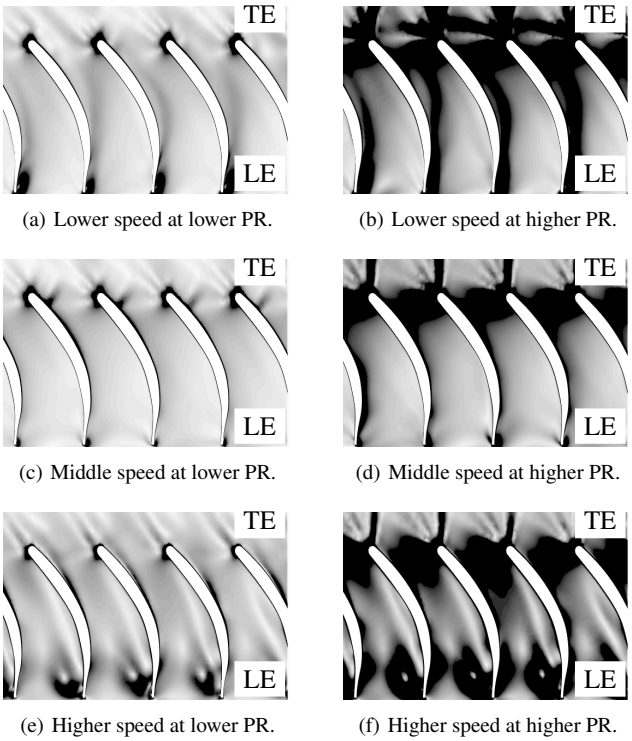

(a) Lower speed at lower PR. (b) Lower speed at higher PR.

(c) Middle speed at lower PR. (d) Middle speed at higher PR.

(e) Higher speed at lower PR. (f) Higher speed at higher PR.

Figure 15. Numerical schlieren of URANS simulations at 50% rotor span with opened VGT position.

lower inlet pressure and lower rotational speed. When the inlet pressure is increased supersonic flow can develop in the rotor as visible in Figure 13 for both simulated speeds. However, the flow is not choked in the rotor. While areas of supersonic flow appear at the TE close to the hub at lower speed, first supersonic flow develops at the shroud at higher speeds. This observation is confirmed by the results of simulations with opened VGT positions, which are depicted in Figure 14. In the selected running conditions, the choking is much more developed at elevated turbine pressure ratios of all three simulated reduced speeds. At lower speed, a damping influence of the tip leakage vortex is clearly visible close to the shroud [40]. High supersonic tip leakage flow passes the tip gap and due to a strong shock, experiences a rough deceleration being retarded to subsonic flow with corresponding Mach number way below the Mach number of the surrounding passage. From there on the flow is not able to reach the sonic limit again. Increasing the pressure ratio, the rotor outlet becomes almost entirely choked and strong TE shock waves are pronounced in the numerical Schlieren in Figure 15-(b). At 50% span these shocks cause a deceleration from supersonic to subsonic flow. On the contrary, with the higher simulated speed at lower turbine pressure ratio, results show mostly supersonic Mach numbers close to the shroud, while the flow near the hub remains subsonic. With increased turbine pressure ratio, the passage becomes fully choked. Nevertheless, a subsonic regime is visible in Figure 14-(f) close to the PS of each blade. This subsonic flow originates from a upstream shock, which develops close to the TE shock, as it can be seen in the numerical Schlieren, Figure 15-(f). At middle speed and low pressure ratio, Figure 14-(c), the mass flow rate through the tip gap is less than in

the case of lower speed due to the the shear force at the tip wall and mostly due to the reduction in the pressure difference driving the flow through the gap [73, 74]. As a consequence, the effects of the leakage flow starts to decrease and a considerable region of the main flow at the shroud accelerates becoming supersonic. When the pressure ratio jumps to a higher value, as visible in Figure 14-(d), the flow in the passage is practically choked. However, a subsonic flow on the PS persists. Overall, the evolution of the choked area of the middle speed represents a superposition of both dynamics, which were seen at the lower and higher speed, with a weaker expression. Hence, a smooth transition from the effects seen at low speed towards the effects seen at high speed seem to happen and no further dynamics need to be considered to fully characterize the choking process in the rotor.

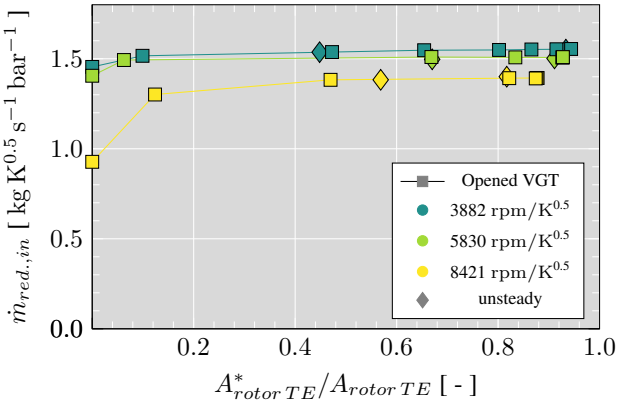

Figure 16. Relation between the reduced mass flow and the area ratio under supersonic conditions.

Figure 16 shows for the steady and unsteady simulation the relation of the ratio between the chocked area and the total area of the rotor TE plane with the reduced mass flow at opened VGT position. It is possible to observe that at lower speed the reduced mass flow stagnates first, which is consistent with the results of Figure 6-(a). Furthermore, it can be notice that as the pressure ratio reach the higher evaluated value in each iso-speed the variation in the area ratio is smaller. The difference in the area ratio between steady and unsteady simulations is due to the effect of the interaction of the flow with the moving blades of the rotor, which is greater at higher speed. Thus, even when the steady simulations can give good results for global parameters, to analyze variables related with the aerodynamic behavior of the flow, as the choked area, unsteady simulations should be carry out. In order to extend the analysis of the choked flow at the rotor, blade-to-blade views with corresponding blade surface pressure profiles are shown for both simulated speeds in Figure 17 for 20%, 50%, and 80% span. At lower speed the flow through the passage seems to be choked at 20% and 50% span, nevertheless at higher speed no choking appears at 20% span, while a much lower intensity of passage choking take place at 50% span. With respect to the corresponding pressure profile these spans are exposed to high positive incidence. This reduces the acceleration on the SS and avoids choking at these spans. The presence of high incidence can be confirmed by the relative inlet flow angle β, presented in Figure 18. At lower speed, the relative inlet flow angle

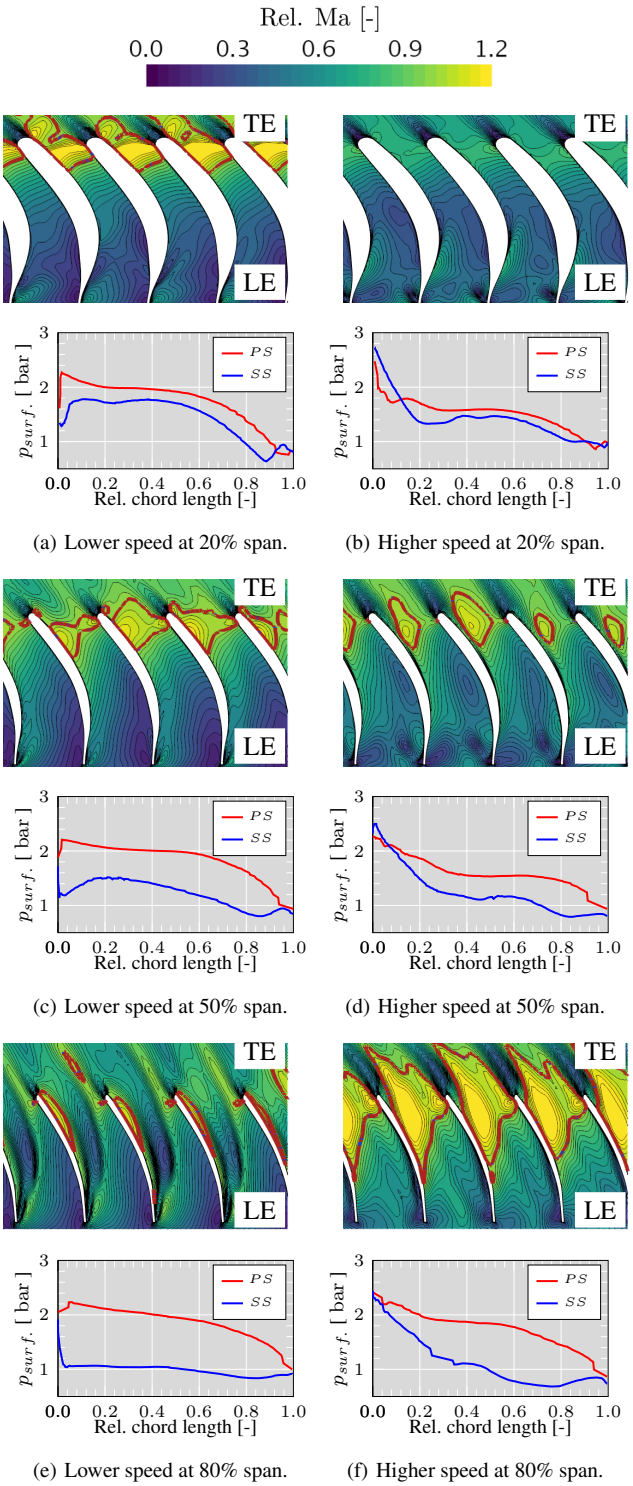

(a) Lower speed at 20% span. (b) Higher speed at 20% span.

(c) Lower speed at 50% span. (d) Higher speed at 50% span.

(e) Lower speed at 80% span. (f) Higher speed at 80% span.

Figure 17. Relative Mach number and rotor pressure profile snapshots at different rotor spans with opened VGT position for lower simulated pressure ratio at lower speed (left) and at higher speed (right); red line: $Ma_{rel.} = 1$.

is close to its optimum value. At higher speed, the high positive incidence is present over the entire circumference and passage height. Nevertheless, the intensity of the positive incidence becomes sightly less towards the hub and shroud due to the secondary flow structures as tip leakage flow in the stator row. The strong impact of secondary flow, as the stator tip leakage vortexes, causes lower β-angle at the

shroud. This might damp the flow acceleration at 80% span less than at lower spans. Additionally, the curvature at higher spans is naturally higher in radial turbines which provokes generally stronger flow acceleration along the same spans. Furthermore, it must be considered that the tip leakage flow [34] and thus, the local avoidance of choking close to the shroud is reduced at higher speeds although the blade loading behaves similar at higher chord lengths. All three effects combined switch the trend that has been observed for lower speed and lead to the observed transition.

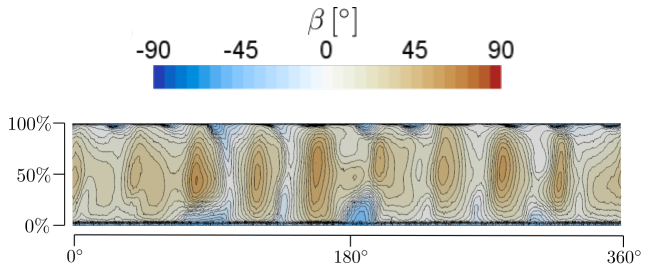

(a) Lower speed at lower PR.

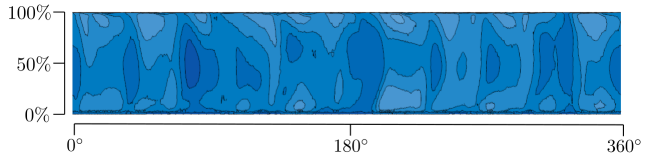

(b) Higher speed at lower PR.

Figure 18. Relative rotor inlet angle snapshots of URANS simulations with opened VGT position and lower simulated pressure ratio of two speeds at the rotor inlet plane.

4.4 *Exergy Analysis*

The specific exergy flow of a perfect gas is defined by the Equation 11,

$$e_f = h_t(T_t) - h_o - T_o\,[s(T_t, p_t) - s_o] \tag{11}$$

$$\Psi = \oiint_{S^*(t)} \left[\rho e_f\,(\vec{u}\cdot\vec{n})\right] dS \tag{12}$$

where h is the specific enthalpy (subscript t denotes the total quantity), s is the specific entropy and T_o is the dead state temperature, Here, the ambient conditions are used as dead state with $T_o = 298.15\,K$ and $p_o = 101325\,Pa$. In order to obtain the net exergy passing through a control surface $S^*(t)$ the Equation 12 has been used, where ρ is the density of the fluid, $\vec{u}$ is the velocity vector of the fluid and $\vec{n}$ is the unit normal vector of $S^*(t)$. The exergy in the inlet duct is evaluated between the inlet probe section (see Figure 2) and the plane at the outlet of the inlet duct. For the volute, the plane at the outlet of the inlet duct and the stator inlet surface are selected, while for the stator and rotor the corresponding inlet and outlet planes in Figure 5-(d) are selected. The vaneless space has been bounded by the stator outlet and the rotor inlet. Finally, the exergy in the outlet was estimated between the rotor outlet surface and the outlet probe section. The Figure 19-(a) shows the results of the exergy normalized by the exergy at the inlet probe section in each region of the computational domain.

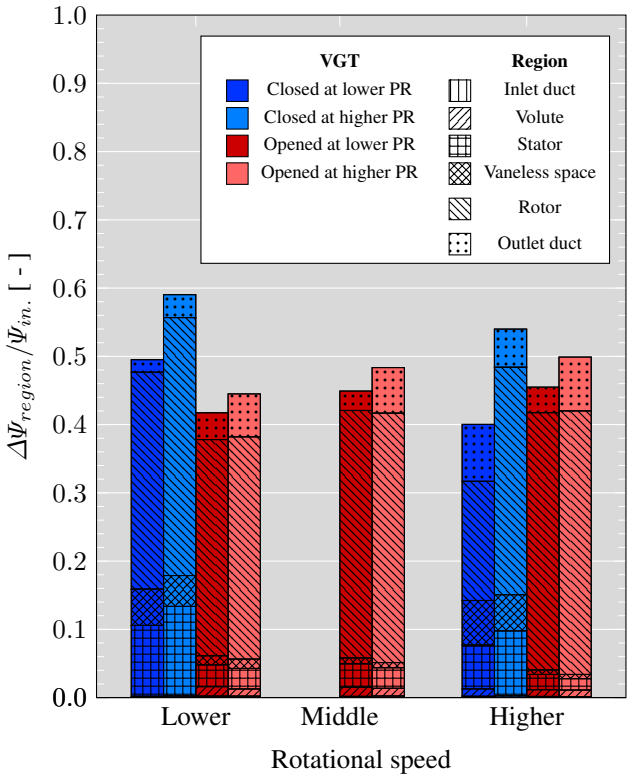

(a) Distribution of the normalized overall exergy in the turbine domain.

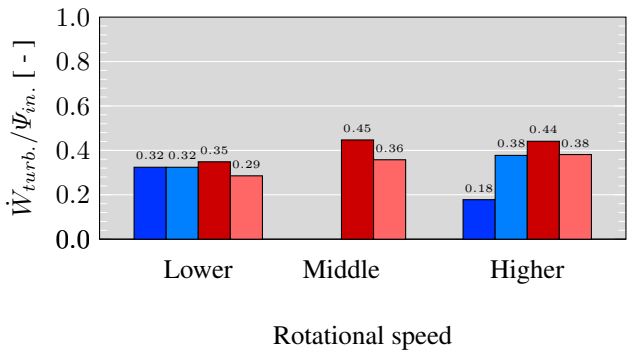

(b) Comparison of the turbine power with respect to the exergy at the inlet probe plane.

Figure 19. Exergy analysis for the evaluated operational points; lower: 3882 $rpm/\sqrt{K}$; middle: 5830 $rpm/\sqrt{K}$; higher: 7456 $rpm/\sqrt{K}$.

The total height of the bar represents the normalized net exergy change within the domain bounded by the inlet probe plane and the outlet probe plane, being a value equal one the maximum reversible work available. The change in the exergy through the inlet duct is negligible and the variation in the volute only represent 1% for the opened VGT position. The fraction corresponding to the stator for the closed VGT is greater than at opened VGT position as it is expected due to the acceleration that suffer the fluid due to the position of the vanes. Furthermore, in this region of the computational domain, with the vanes closed the fraction of the exergy increases 3% points when the pressure ratio is increased at both rotational speed (lower and higher). The maximum change corresponds to the case of lower speed and higher pressure ratio, which is consistent due the presence of a

stronger shock as is depicted in Figure 11-(d). Regarding to the exergy in the vaneless space, this one is significant at closed VGT position due to the interaction between the rotor and stator which increase the irreversibilities. The bigger fraction of the exergy budget corresponds to the rotor. The remaining fraction corresponds to the outlet representing the entropy generated be the swirl of the flow just at the rotor outlet. It is worth mentioned that the flow exergy loss due to internal irreversibilities can be may due to the entropy generation of viscous friction and the heat transfer across finite temperature difference. Thus, as the presented study is under adiabatic conditions and low inlet temperature the viscous irreversibilities are more significant than the thermal irreversibilities. The ratio of the turbine power over the exergy flow between the inlet probe section and the outlet probe section was calculated for each operation points and is presented in the Figure 19-(b). For the closed VGT position, it is possible to observe that at lower speed the turbine power extracted form the maximum energy available at the inlet does not change significantly when the pression ratio increases which is in concordance with the small change in the efficiency depicted in Figure 6-(b). The biggest approach of the maximum energy corresponds to the case of opened VGT at lower pressure ratio and middle speed.

5 Conclusions and Future Work

For the turbine geometry considered in this study at a closed position of the stator vanes, a shock develops first on the SS of the stator vanes and not in the perpendicular section that goes from the TE of one vane until the SS of the neighboring vane, which is considered as the geometrical throat of the stator in the literature, despite of the reduced area between the vanes. At turbine pressure ratios around 5, the full stator choking is achieved in the throat of the vaneless space just upstream of the rotor inlet. This avoids the rotor-stator interaction with the developed shock at the stator SS. With increasing turbine pressure ratio a partially choked rotor outlet has been identified at already choked vaneless space throat. When stator vanes are opened, choking occurs only in the rotor throat close to the rotor outlet. It has been found that the stagnation of reduced mass flow in the rotor outlet appears at different values. In the mostly choked rotor outlet the flow reaches supersonic speeds above 1. At lower turbine speeds the tip leakage flow has been identified to be responsible for subsonic regions in the rotor TE plane, although the passage is mainly choked. Tip leakage flow is likely to overpass the tip gap with high supersonic speed and experiences a rough deceleration due to a strong shock. According to Equation 6 and assuming that the tip leakage flow reduces the Mach number in the rotor outlet, the reduced mass flow based on Equation 10 increases for lower speeds where stronger tip leakage flow can be identified. It has been shown that this effect can increase the spreading of the speed lines in the overall reduced mass flow map. Furthermore, it has been found that the total pressure ratio and the total temperature difference between turbine inlet and turbine outlet maintains constant at a similar turbine pressure ratio as the highest reduced mass flow has been identified. This demonstrates the aerodynamic choking of the overall passage flow (excluding the tip leakage flow). Additionally, different trends depending on the rotational velocity were identified for the development of rotor passage choking. At lower speeds the effectively choked area arises at the rotor hub and expands towards the shroud. This evolution is related with the choking delay close to shroud provoked by the tip leakage vortex. At higher speed, the strength of the tip leakage vortex is expected to be lower. Thus, the choking at higher spans is not equally damped as at lower speed. The naturally higher blade curvature at high spans in radial turbines favors the flow acceleration resulting in earlier passing of the sonic limit. At the same time the flow enters with high positive incidence at low spans. The relative inflow angle damps the acceleration along the SS at lower spans. An exergy analysis was carry out in order to quantify the fraction of reversible work available in each region. The greater change of the exergy occurs in the rotor. The fractions in the stator and vaneless space are representatives at closed VGT and increase as the pressure ratio increases which is also related with intensity of the choked flow. The biggest approach of the maximum amount of shaft work that can be extracted from the conditions of the fluid at the inlet until its equilibrium with the environment, corresponds to the oprataional point at opened VGT lower pressure and middle speed. These result can be used in future work to quantify and identify the regions with the higher internal irrevesibilities in order to improve the performance of the turbine. The findings of this paper are useful to develop physical one-dimensional models to extrapolate the turbine map toward high pressure ratios. Here, the turbine will be considerate as an equivalent nozzle taking into account the VGT position, rotational speed, pressure ratio, inlet flow conditions as the mass flow as well as geometrical parameters. The model will evaluate the pressure ratio when the shocking appears first in the stator or in the rotor. Afterward, with all this data the model will use the definition of the critical mass flow through an isentropic nozzle to find an equivalent area, which will be recalculated following an iteration process and coefficients fitting. Once the equivalent area has been calculated the reduced mass flow can be interpolated or extrapolated in order to get the turbine map. Nevertheless, this is a previous idea of the model and certain modifications can occur during the development and implementation process. Due to the significant influence of the tip leakage flow on the choking behavior in the rotor exit, further studies will be planned to enhance the aforementioned one-dimensional modeling. In addition, the aerodynamic phenomenon presented has to be taken into account in the early phase of the design. The results will further guide experimental measurements, which will be executed in the future. These experiments will further be applied as experimental validation of the numerical results.

Acknowledgements

The work has been partially supported by the "Subprograma de Formación de Profesorado Universitario (FPU)". Ministerio de Universidades. FPU18/02628 and by the "FPI Subprograma 2". Universitat Politècnica de València. PAID-10-18.

6 Declaration of conflicting interests

The author(s) declared no potential conflicts of interest with respect to the research, authorship and/or publication of this article.

References

1. Europian Parlament. Regulation (EU) 2016/1628 of the European Parliament and of the Council of 14 September 2016 on requirements relating to gaseous and particulate pollutant emission limits and type approval for internal combustion engines for non-road mobile machinery, 2016. URL http://data.europa.eu/eli/reg/2016/1628/2020-07-01.
2. Europian Parlament. Regulation (EU) 2020/1040 of the European Parliament and of the Council of 15 July 2020 amending Regulation (EU) 2016/1628 as regards its transitional provisions in order to address the impact of the COVID-19 crisis (Text with EEA relevance), 2020. URL https://eur-lex.europa.eu/eli/reg/2020/1040/oj?eliuri=eli:reg:2020:1040:oj{&}print=true.
3. Cheng L, Dimitriou P, Wang W et al. A novel fuzzy logic variable geometry turbocharger and exhaust gas recirculation control scheme for optimizing the performance and emissions of a diesel engine. *International Journal of Engine Research* 2020; 21(8): 1298–1313. DOI:10.1177/1468087418809261. URL https://doi.org/10.1177/1468087418809261.
4. Song K, Upadhyay D and Xie H. An assessment of the impacts of low-pressure exhaust gas recirculation on the air path of a diesel engine equipped with electrically assisted turbochargers. *International Journal of Engine Research* 2021; 22(1): 3–21. DOI:10.1177/1468087419854294. URL https://doi.org/10.1177/1468087419854294.
5. Turner JW, Popplewell A, Richardson S et al. Ultra boost for economy: Realizing a 60% downsized engine concept. In *Internal Combustion Engines: Performance, Fuel Economy and Emissions*. London, UK: Woodhead Publishing. ISBN 9781782421849, 2013. pp. 3–17. DOI:10.1533/9781782421849.1.3. URL http://www.sciencedirect.com/science/article/pii/B9781782421832500019.
6. Carey C, McAllister M, Sandford M et al. Extreme engine downsizing. In *Innovations in Fuel Economy and Sustainable Road Transport*. Woodhead Publishing. ISBN 9780857092137, 2011. pp. 135–147. DOI:10.1533/9780857095879. URL http://www.sciencedirect.com/science/article/pii/B9780857092137500127.
7. Romagnoli A, Wan-Salim WS, Gurunathan BA et al. Assessment of supercharging boosting component for heavily downsized gasoline engines. In *11th International Conference on Turbochargers and Turbocharging*. Oxford: Woodhead Publishing. ISBN 9780081000335, 2014. pp. 13–26. DOI:10.1533/978081000342.13. URL http://www.sciencedirect.com/science/article/pii/B9780081000335500020.
8. Hu B, Brace C, Akehurst S et al. The effect of divided exhaust period for improved performance in a highly downsized turbocharged gasoline engine. In Engineers IoM (ed.) *11th International Conference on Turbochargers and Turbocharging*. Oxford: Woodhead Publishing. ISBN 9780081000335, 2014. pp. 27–39. DOI:10.1533/978081000342.27. URL http://www.sciencedirect.com/science/article/pii/B9780081000335500032.
9. de Bellis V, Bozza F, Marelli S et al. Experimental Investigation and 1D Simulation of a Turbocharger Compressor Close to Surge Operation. *SAE International Journal of Engines* 2015; 8(4). DOI:10.4271/2015-01-1720. URL https://doi.org/10.4271/2015-01-1720.
10. Mirza-Hekmati D, Heath WP, Apsley JM et al. Downspeeding diesel engines with two-stage turbochargers: Analysis and control considerations. *International Journal of Engine Research* 2020; : 1–12DOI:10.1177/1468087420976482. URL https://doi.org/10.1177/1468087420976482.
11. Huayin T. *Application of Variable Geometry Turbine on Gasoline Engines and the Optimisation of Transient Behaviours*. PhD Thesis, University of Bath, 2016. URL https://researchportal.bath.ac.uk/en/studentTheses/application-of-variable-geometry-turbine-on-gasoline-engines-and-.
12. Tang H, Akehurst S, Brace CJ et al. Optimisation of transient response of a gasoline engine with variable geometry turbine turbocharger. In Engineers IoM (ed.) *11th International Conference on Turbochargers and Turbocharging*. Oxford: Woodhead Publishing. ISBN 9780081000335, 2014. pp. 163–175. DOI:10.1533/978081000342.163. URL http://www.sciencedirect.com/science/article/pii/B9780081000335500147.
13. Kawakubo T. Unsteady Rotor-Stator Interaction of a Radial-Inflow Turbine With Variable Nozzle Vanes. In *Proceedings of ASME Turbo Expo 2010: Power for Land, Sea and Aiar*. Glasgow, UK, pp. 2075–2084. DOI:10.1115/GT2010-23677. URL https://doi.org/10.1115/GT2010-23677.
14. Sato W, Yamagata A and Hattori H. A Study of Aerodynamic Excitation Forces on a Radial Turbine Blade Due to Rotor-Stator Interaction. In Engineers IoM (ed.) *Institution of Mechanical Engineers - 11th International Conference on Turbochargers and Turbocharging*. Oxford: Woodhead Publishing. ISBN 9780081000335, pp. 389–398. URL http://www.sciencedirect.com/science/article/pii/B9780081000335500317.
15. Zhao B, Sun H, Shi X et al. Investigation of using multi-shockwave system instead of single normal shock for improving radial inflow turbine reliability. *International Journal of Heat and Fluid Flow* 2018; 71(March): 170–178. DOI:10.1016/j.ijheatfluidflow.2018.03.018. URL http://www.sciencedirect.com/science/article/pii/S0142727X17305507.
16. Yang D, Lao D, Yang C et al. Investigations on the Generation and Weakening of Shock Wave in a Radial Turbine With Variable Guide Vanes, 2016. DOI:10.1115/GT2016-57047. URL https://doi.org/10.1115/GT2016-57047.
17. Hu L, Yang C, Sun H et al. Numerical Analysis of Nozzle Clearance's Effect on Turbine Performance. *Chinese Journal of Mechanical Engineering* 2011; 24(4): 618–625. DOI:10.3901/CJME.2011.04.618. URL http://www.cjmenet.com/article/id/e41481ab-f2b8-4808-bd23-96d74a486da9?pageType=en.

18. Zhao B, Yang C, Hu L et al. Understanding of the Interaction between Clearance Leakage Flow and Main Passage Flow in a VGT Turbine. *Advances in Mechanical Engineering* 2015; 7(2): 652769. DOI:10.1155/2014/652769. URL https://doi.org/10.1155/2014/652769.
19. Liu Y, Lao D, Liu Y et al. Investigation on the effects of nozzle openings for a radial turbine with variable nozzle. In *SAE 2014 World Congress & Exhibition*, volume 01. Detroit, United Staes: SAE International. ISBN 2014011648, pp. 1–8. DOI:10.4271/2014-01-1648. URL https://doi.org/10.4271/2014-01-1648.
20. Hu L, Sun H, Yi J et al. Investigation of nozzle clearance effects on a radial turbine: Aerodynamic performance and forced response. In *SAE 2013 World Congress & Exhibition*, volume 1. Detroit, United Staes: SAE International, pp. 1–11. DOI:10.4271/2013-01-0918. URL https://doi.org/10.4271/2013-01-0918.
21. Paniagua G, Yasa T, De La Loma A et al. Unsteady strong shock interactions in a transonic turbine: Experimental and numerical analysis. *Journal of Propulsion and Power* 2008; 24(4): 722–731. DOI:10.2514/1.34774. URL https://doi.org/10.2514/1.34774.
22. Chen H. Turbine wheel design for Garrett advanced variable geometry turbines for commercial vehicle applications. In Institution of Mechanical Engineers Combustion Engines & Fuels Group BTtICoT and Turbocharging (eds.) *8th International Conference on Turbochargers and Turbocharging*. Woodhead Publishing. ISBN 1845691741, 2006. pp. 317–327. DOI:10.1533/9781845697099.6.317. URL http://www.sciencedirect.com/science/article/pii/B9781845691745500270.
23. *Secondary Flow Structures and Losses in a Radial Turbine Nozzle*, *Turbo Expo: Power for Land, Sea, and Air*, volume Volume 3:, 2011. DOI:10.1115/GT2011-46753. URL https://doi.org/10.1115/GT2011-46753.
24. Heuer T, Gugau M, Klein A et al. An analytical approach to support high cycle fatigue validation for turbocharger turbine stages. In *Turbo Expo: Power for Land, Sea, and Air*, volume 1. Berlin, Germany: ASME. ISBN 9780791843116, pp. 723–732. DOI:10.1115/GT2008-50764. URL https://doi.org/10.1115/GT2008-50764.
25. Rubechini F, Marconcini M, Arnone A et al. Special Challenges in the CFD Modeling of Transonic Turbo-Expanders. In *ASME Turbo Expo 2013: Turbine Technical Conference and Exposition*. San Antonio, Texas, USA: ASME, pp. 1–10. DOI:10.1115/GT2013-95554. URL https://doi.org/10.1115/GT2013-95554.
26. Allport JM, Jupp ML, Pezouvanis A et al. Turbocharger blade vibration: Measurement and validation through laser tip-timing. In IMechE (ed.) *10th International Conference on Turbochargers and Turbocharging*. 2, Woodhead Publishing. ISBN 9780857092090, 2012. pp. 173–181. DOI:10.1533/9780857096135.3b.173. URL http://www.sciencedirect.com/science/article/pii/B9780857092090500145.
27. Bachschmid N, Pesatori E, Bistolfi S et al. Blade Vibration Measurements and Excitation Force Evaluation. In Pennacchi P (ed.) *Proceedings of the 9th IFToMM International Conference on Rotor Dynamics*. Cham: Springer International Publishing. ISBN 978-3-319-06590-8, pp. 65–78. URL https://link.springer.com/chapter/10.1007/978-3-319-06590-8{_}6.
28. Sauret E. Open Design of High Pressure Ratio Radial-Inflow Turbine for Academic Validation. In ASME (ed.) *Proceedings of the ASME 2012 International Mechanical Engineering Congress and Exposition*, volume 7. Houston, USA, pp. 3183–3197. DOI:10.1115/IMECE2012-88315. URL https://doi.org/10.1115/IMECE2012-88315.
29. Izaguirre AOT, García RN, Inhestern LB et al. Design and numerical analysis of flow characteristics in a scaled volute and vaned nozzle of radial turbocharger turbines. *Energies* 2020; 13(11): 19. DOI:10.3390/en13112930. URL https://doi.org/10.3390/en13112930.
30. Dufour G, Carbonneau X, Cazalbou Jb et al. Practical Use of Similarity and Scaling Laws for Centrifugal Compressor Design. In *Turbo Expo: Power for Land, Sea, and Air*, volume 6. Barcelona, Spain: ASME, pp. 1131–1140. DOI:10.1115/GT2006-91227. URL https://doi.org/10.1115/GT2006-91227.
31. Galindo J, Tiseira Izaguirre AO, García-Cuevas LM et al. Experimental approach for the analysis of the flow behaviour in the stator of a real centripetal turbine. *International Journal of Engine Research* 2020; 0: 1–11. DOI:10.1177/1468087420916281. URL https://doi.org/10.1177/1468087420916281.
32. Serrano JR, Gil A, Navarro R et al. Extremely low mass flow at high blade to jet speed ratio in variable geometry radial turbines and its influence on the flow pattern a CFD analysis. In *ASME Turbo Expo 2017: Turbomachinery Technical Conference and Exposition*. Charlotte, NC, USA: ASME, pp. 1–13. DOI:10.1115/GT2017-63368. URL https://asmedigitalcollection.asme.org/GT/proceedings-abstract/GT2017/50954/V008T26A005/243279.
33. Kammeyer, Jasper and Natkaniec, Christoph and Seume JR. Tip leakage in small radial turbines: Optimum tip-gap and efficiency loss correlations. In *Turbo Expo: Power for Land, Sea, and Air*. Glasgow, UK: ASME, pp. 1–11. DOI:10.1115/GT2010-22680. URL https://doi.org/10.1115/GT2010-22680.
34. Serrano JR, Navarro R, García-Cuevas LM et al. Contribution to tip leakage loss modeling in radial turbines based on 3D flow analysis and 1D characterization. *International Journal of Heat and Fluid Flow* 2019; 78: 1–7. DOI:10.1016/j.ijheatfluidflow.2019.108423. URL http://www.sciencedirect.com/science/article/pii/S095559861530042X.
35. Serrano JR, Arnau FJ, García-Cuevas LM et al. Development and validation of a radial turbine efficiency and mass flow model at design and off-design conditions. *Energy Conversion and Management* 2016; 128: 281–293. DOI:10.1016/j.enconman.2016.09.032. URL https://doi.org/10.1016/j.enconman.2016.09.032.
36. Romagnoli A and Martinez-Botas R. Performance prediction of a nozzled and nozzleless mixed-flow turbine in steady conditions. *International Journal of Mechanical Sciences* 2011; 53(8): 557–574. DOI:10.1016/j.ijmecsci.2011.05.003. URL http://www.sciencedirect.com/science/article/pii/S0020740311000920.
37. Meroni A, Robertson M, Martinez-Botas R et al. A methodology for the preliminary design and performance prediction of high-pressure ratio radial-inflow turbines. *Energy* 2018;

164: 1062–1078. DOI:10.1016/j.energy.2018.09.045. URL https://doi.org/10.1016/j.energy.2018.09.045.

38. Tancrez M, Galindo J, Guardiola C et al. Turbine adapted maps for turbocharger engine matching. *Experimental Thermal and Fluid Science* 2011; 35(1): 146–153. DOI:10.1016/j.expthermflusci.2010.07.018. URL http://dx.doi.org/10.1016/j.expthermflusci.2010.07.018.
39. Zamboni G, Moggia S and Capobianco M. Effects of a dual-loop exhaust gas recirculation system and variable nozzle turbine control on the operating parameters of an automotive diesel engine. *Energies* 2017; 10(1): 47. DOI:10.3390/en10010047. URL https://doi.org/10.3390/en10010047.
40. Serrano JR, Navarro R, García-Cuevas LM et al. Turbocharger turbine rotor tip leakage loss and mass flow model valid up to extreme off-design conditions with high blade to jet speed ratio. *Energy* 2018; 147: 1299–1310. DOI:https://doi.org/10.1016/j.energy.2018.01.083. URL https://www.sciencedirect.com/science/article/pii/S0360544218301014.
41. SAE. Turbocharger Gas Stand Test Code, 1995. DOI:10.4271/J1826_199503. URL https://doi.org/10.4271/J1826{_}199503.
42. Serrano JR, Tiseira A, García-Cuevas LM et al. Radial turbine performance measurement under extreme off-design conditions. *Energy* 2017; 125: 72–84. DOI:10.1016/j.energy.2017.02.118. URL http://www.sciencedirect.com/science/article/pii/S0360544217303018.
43. Siemens. STAR-CCM + 2019.1 Release version 14.02.010-R8., 2019. URL https://www.plm.automation.siemens.com/global/es/products/simcenter/STAR-CCM.html.
44. Menter FR. Two-equation eddy-viscosity turbulence models for engineering applications. *AIAA Journal* 1994; 32(8): 1598–1605. DOI:10.2514/3.12149. URL https://doi.org/10.2514/3.12149.
45. Menter FR, Langtry R and Hansen T. CFD simulation of turbomachinery flows - Verfication, validation and modelling. In *ECCOMAS 2004 - European Congress on Computational Methods in Applied Sciences and Engineering*. July, Jyväskylä, pp. 1–14. URL http://www.mit.jyu.fi/eccomas2004/proceedings/pdf/954.pdf.
46. Simpson AT, Spence SWT and Watterson JK. A Comparison of the Flow Structures and Losses Within Vaned and Vaneless Stators for Radial Turbines. *Journal of Turbomachinery* 2009; 131(3). DOI:10.1115/1.2988493. URL https://doi.org/10.1115/1.2988493.
47. Galindo J, Fajardo P, Navarro R et al. Characterization of a radial turbocharger turbine in pulsating flow by means of CFD and its application to engine modeling. *Applied Energy* 2013; 103: 116–127. DOI:10.1016/j.apenergy.2012.09.013. URL http://dx.doi.org/10.1016/j.apenergy.2012.09.013.
48. Xue Y, Yang M, Pan L et al. Gasdynamic behaviours of a radial turbine with pulsating incoming flow. *Energy* 2021; 218: 119523. DOI:10.1016/j.energy.2020.119523. URL http://www.sciencedirect.com/science/article/pii/S036054422032630X.
49. Zhao B, Qi M, Sun H et al. A comprehensive analysis on the structure of groove-induced shock waves in a linear turbine. *Aerospace Science and Technology* 2019; 87(1270-9638): 331–339. DOI:10.1016/j.ast.2019.02.036. URL http://www.sciencedirect.com/science/article/pii/S1270963818320388.
50. Ananthakrishnan K and Govardhan M. Influence of fillet shapes on secondary flow field in a transonic axial flow turbine stage. *Aerospace Science and Technology* 2018; 82-83: 425–437. DOI:https://doi.org/10.1016/j.ast.2018.08.040. URL https://www.sciencedirect.com/science/article/pii/S1270963818307533.
51. Balasubramanian R, Barrows S and Chen JP. *Investigation of shear-stress transport turbulence model for turbomachinery applications*. January, Amercian Institute of Aeronautics and Astronautics, 2008. ISBN 9781563479373. DOI:10.2514/6.2008-566. URL https://arc.aiaa.org/doi/abs/10.2514/6.2008-566.
52. Menter FR. Review of the shear-stress transport turbulence model experience from an industrial perspective. *International Journal of Computational Fluid Dynamics* 2009; 23(4): 305–316. DOI:10.1080/10618560902773387. URL https://doi.org/10.1080/10618560902773387.
53. Ram P, Kim T and Kim HD. Numerical Study on Shock Train Characteristics in Divergent Channels. *Journal of Applied Fluid Mechanics* 2020; 13: 1081–1092. DOI:10.36884/jafm.13.04.30837. URL https://doi.org/10.36884/jafm.13.04.30837.
54. Zheltovodov A. Shock waves/turbulent boundary-layer interactions - Fundamental studies and applications. In *Fluid Dynamics Conference*. New Orleans: AIAA, pp. 1–28. DOI:10.2514/6.1996-1977. URL https://arc.aiaa.org/doi/abs/10.2514/6.1996-1977.
55. Bardina JE, Huang PG and Coakley TJ. *Turbulence modeling validation*. National Aeronautics and Space Administration, 1997. DOI:10.2514/6.1997-2121. URL https://arc.aiaa.org/doi/abs/10.2514/6.1997-2121.
56. Galindo J, Hoyas S, Fajardo P et al. Set-Up Analysis and Optimization of CFD Simulations for Radial Turbines. *Engineering Applications of Computational Fluid Mechanics* 2013; 7(4): 441–460. DOI:10.1080/19942060.2013.11015484. URL https://doi.org/10.1080/19942060.2013.11015484.
57. Hazizi, Kristaq and Ramezanpour, Ahad and Costall, Aaron and Asadi M. Numerical analysis of a turbocharger compressor. In *XII International Conference on Computational Heat, Mass and Momentum Transfer (ICCHMT 2019)*, volume 128. E3S Web of Conferences, pp. 1–8. DOI:10.1051/e3sconf/201912806012. URL https://doi.org/10.1051/e3sconf/201912806012.
58. Harinck J, Turunen-Saaresti T, Colonna P et al. Computational Study of a High-Expansion Ratio Radial Organic Rankine Cycle Turbine Stator. *Journal of Engineering for Gas Turbines and Power* 2010; 132(5). DOI:10.1115/1.3204505. URL https://doi.org/10.1115/1.3204505.
59. Sauret E and Gu Y. Three-dimensional off-design numerical analysis of an organic Rankine cycle radial-inflow turbine. *Applied Energy* 2014; 135: 202–211. DOI:10.1016/j.apenergy.2014.08.076. URL https://www.sciencedirect.com/science/article/pii/S0306261914008873.
60. Li S, Wang S, Ma Z et al. An air cycle heat pump heating system using a turbocharger for full electric

vehicle. *Procedia Engineering* 2017; 205: 1405–1411. DOI:https://doi.org/10.1016/j.proeng.2017.10.316. URL https://www.sciencedirect.com/science/article/pii/S1877705817349810.

61. Li S, Wang S, Ma Z et al. Using an air cycle heat pump system with a turbocharger to supply heating for full electric vehicles. *International Journal of Refrigeration* 2017; 77: 11–19. DOI:https://doi.org/10.1016/j.ijrefrig.2017.03.004. URL https://www.sciencedirect.com/science/article/pii/S0140700717300993.
62. Pérez-Grande I and Leo TJ. Optimization of a commercial aircraft environmental control system. *Applied Thermal Engineering* 2002; 22(17): 1885–1904. DOI: https://doi.org/10.1016/S1359-4311(02)00130-8. URL https://www.sciencedirect.com/science/article/pii/S1359431102001308.
63. Yang H, Zhang X, Wang C et al. Experimental and theoretical study on a novel energy-saving ECS for commercial airliners. *Applied Thermal Engineering* 2017; 127: 1372–1381. DOI:https://doi.org/10.1016/j.applthermaleng.2017.08.043. URL http://www.sciencedirect.com/science/article/pii/S1359431117324596.
64. Drela M and Youngren H. *A User's Guide to MISES 2.63*. February, MIT Aerospace Computational Design Laboratory, 2008. URL http://web.mit.edu/drela/Public/web/mises/mises.pdf.
65. Serrano JR, Arnau FJ, García-Cuevas LM et al. An innovative losses model for efficiency map fitting of vaneless and variable vaned radial turbines extrapolating towards extreme off-design conditions. *Energy* 2019; 180: 626–639. DOI:10.1016/j.energy.2019.05.062. URL http://www.sciencedirect.com/science/article/pii/S0360544219309314.
66. Filipi Z, Wang Y and Assanis D. Effect of variable geometry turbine (VGT) on diesel engine and vehicle system transient response. In *SAE 2001 World Congress*. 724, SAE International, pp. 1–21. DOI:10.4271/2001-01-1247. URL https://doi.org/10.4271/2001-01-1247.
67. Rogo C, Hájek T and Chen AG. *Variable stator radial turbine*. NASA United States, 1984. DOI:9840014500. URL https://ntrs.nasa.gov/search.jsp?R=19840014500.
68. Yaras MI and Sjolander SA. Prediction of Tip-Leakage Losses in Axial Turbines. *Journal of Turbomachinery* 1992; 114(1): 204–210. DOI:10.1115/1.2927987. URL https://doi.org/10.1115/1.2927987.
69. Pohl D, Janssen J, Jeschke P et al. Variable Stator Vane Penny Gap Aerodynamic Measurements and Numerical Analysis in an Annular Cascade Wind Tunnel. *International Journal of Gas Turbine, Propulsion and Power Systems* 2020; 11(2): 44–55. DOI:https://doi.org/10.38036/jgpp.11.2_44. URL http://www.gtsj.org/english/index.html.
70. Stummann S, Pohl D, Jeschke P et al. Secondary Flow in Variable Stator Vanes With Penny-Cavities. In *ASME Turbo Expo 2017: Turbomachinery Technical Conference and Exposition*, volume Volume 2A:. Charlotte, North Carolina, USA: ASME. ISBN 978-0-7918-5078-7, pp. 1–12. DOI:10.1115/GT201763771. URL https://doi.org/10.1115/GT2017-63771.
71. Japikse D and Baines N. *Introduction to Turbomachinery*. Concepts ETI, Inc, 1994.
72. Denton JD. Loss mechanisms in turbomachines. *Journal of Turbomachinery* 1993; 115((Cambridge, U.K.: Sep. 1-3, 1987), Bury St. Edmunds, U.K., Mech. Engng. Publications Ltd., 1987, Pap): 621–656. DOI:10.1115/1.2929299. URL https://doi.org/10.1115/1.2929299.
73. Yaras MI and Sjolander SA. Effects of simulated rotation on tip leakage in a planar cascade of turbine blades: Part I: Tip gap flow. *Journal of Turbomachinery* 1992; 114(3): 652–659. DOI: 10.1115/1.2929189. URL https://doi.org/10.1115/1.2929189.
74. Yaras MI and Sjolander SA. Effects of Simulated Rotation on Tip Leakage in a Planar Cascade of Turbine Blades: Part II—Downstream Flow Field and Blade Loading. *Journal of Turbomachinery* 1992; 114(3): 660–667. DOI: 10.1115/1.2929190. URL https://doi.org/10.1115/1.2929190.